Electronic Supplementary Information

Ion-Conductive Crystals of Poly (vinylidene fluoride) Enables Fast Charging Solid-State Lithium Metal Batteries

Chen Dai,[a,#] Mowei Weng,[a,#] Bowen Cai,[a,#] Junfeng Liu, [a] Shaoke Guo,[b] Hao Xu,[b] Lei Yao,[a] Florian J. Stadler,[a] Zhong-Ming Li,[c] and Yan-Fei Huang [a,]*

[a] *Guangdong Provincial Key Laboratory of New Energy Materials Service Safety, College of Materials Science and Engineering, Shenzhen University, 518060, P. R. China*

[b] *Shenzhen All-Solid-State Lithium Battery Electrolyte Engineering Research Center, Institute of Materials Research (IMR), Tsinghua Shenzhen International Graduate School, Tsinghua University, Shenzhen 518055, China*

[c] *College of Polymer Science and Engineering and State Key Laboratory of Polymer Materials Engineering, Sichuan University, 610065, P. R. China*

Corresponding author: yanfeihuang@szu.edu.cn

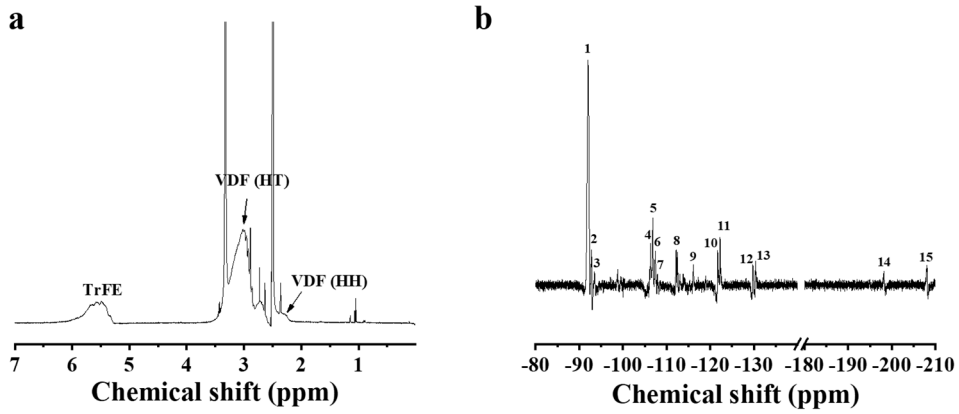

Figure S1. (a) ^{1}H and (b) ^{19}F NMR spectra (DMSO-d_6) for the *d*-PVDF terpolymer.

Table S1. The peak assignments of ^{19}F NMR results of the *d*-PVDF.

Peak NO.	Sequence	Designation	Chemical Shift (ppm)
1	-$CF_2CH_2CF_2CH_2CF_2$-	H-T	-92.04
2	-$CF_2CH_2CF_2CH_2CF_2$-	H-T	-92.80
3	-$CClFCH_2CF_2CH_2CH_2$-	T-T	-93.34~-93.66
	-$CHFCH_2CF_2CH_2CF_2$-	T-T	
4	-$CH_2CClFCH_2CClFCH_2$-	H-T	-106.34
5	-$CF_2CHFCF_2CH_2CF_2$-	H-T	-106.79
6	-$CH_2CH_2CF_2CHFCF_2$-	H-T	-107.40
7	-$CF_2CH_2CF_2CH_2CClF$-	T-T	-107.80
8	-$CF_2CH_2CF_2CF_2CHF$-	T-T	-112.15~-112.44
9	-$CF_2CH_2CF_2CH_2CF_2$-	T-T	-116.07
10	-$CF_2CHFCF_2CHFCF_2$-	H-T	-121.68
11	-$CHFCHFCF_2CF_2CHF$-	T-T	-122.31
12	-$CH_2CF_2CF_2CHFCH_2$-	H-H	-129.72
13	-$CH_2CFClCF_2CHFCH_2$-	H-T-T	-130.42
14	-$CF_2CF_2CHFCH_2CF_2$-	T-T	-198.19
15	-$CH_2CF_2CHFCF_2CH_2$-	H-T	-208.04

Note: Peak assignments are referenced from: Y. Y. Lu, J. Claude, Q.-M. Zhang, Q. Wang, *Macromolecule*s **2006,** 39, 6962; Zhang, G. Z.; G. Z. Zhang, Q. Li, H. M. Gu, S. L. Jiang, K. Han, M. R. Gadinski, M. A. Haque, Q. M. Zhang, Q. Wang, *Adv. Mater.* **2015**, 27, 1450.

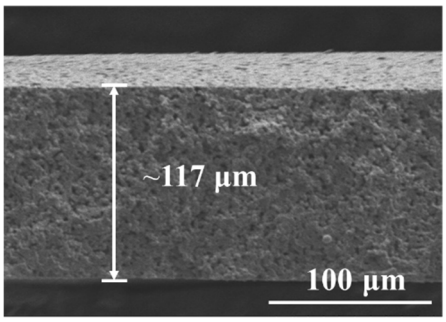

Figure S2. The SEM image of the cross-section of PVDF SPEs.

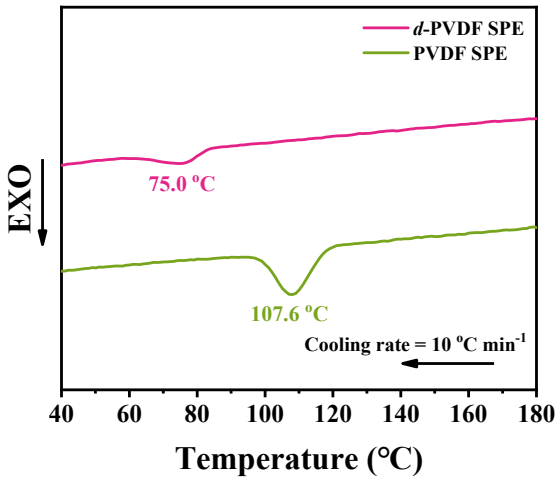

Figure S3. DSC cooling curves of *d*-PVDF SPE and PVDF SPE.

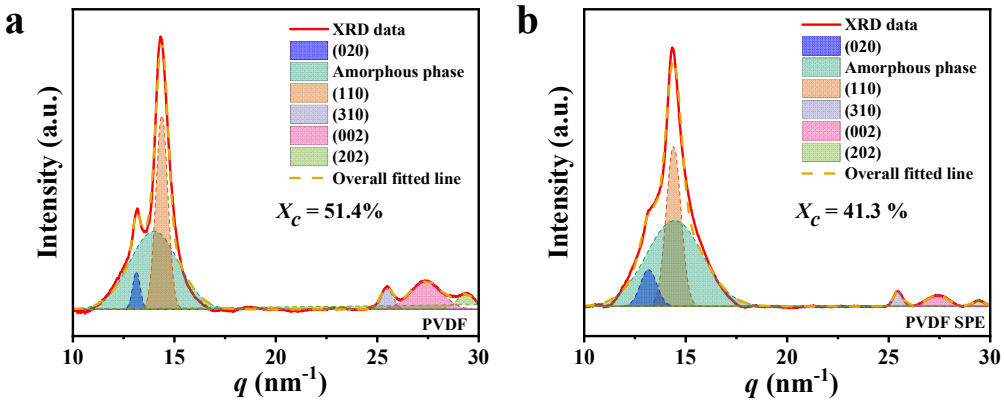

Figure S4. Peak-fitting of 1D fiber XRD curves of (a) PVDF and (b) PVDF SPEs to calculate the crystallinity.

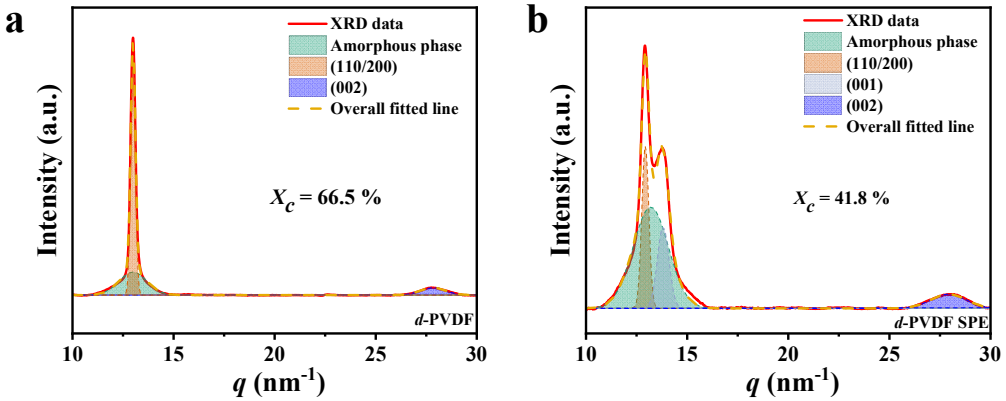

Figure S5. Peak-fitting of 1D fiber XRD curves of (a) *d*-PVDF and (b) *d*-PVDF SPEs to calculate the crystallinity.

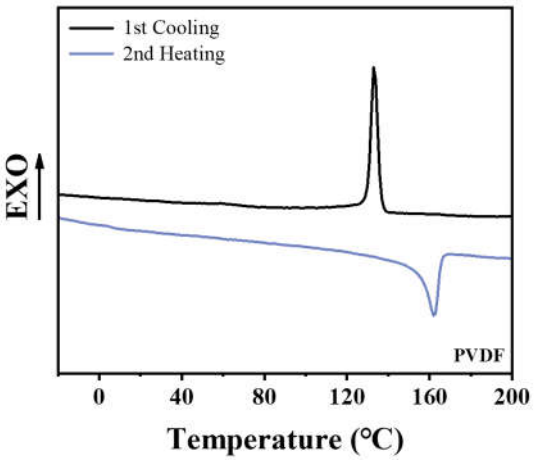

Figure S6. DSC curves of PVDF.

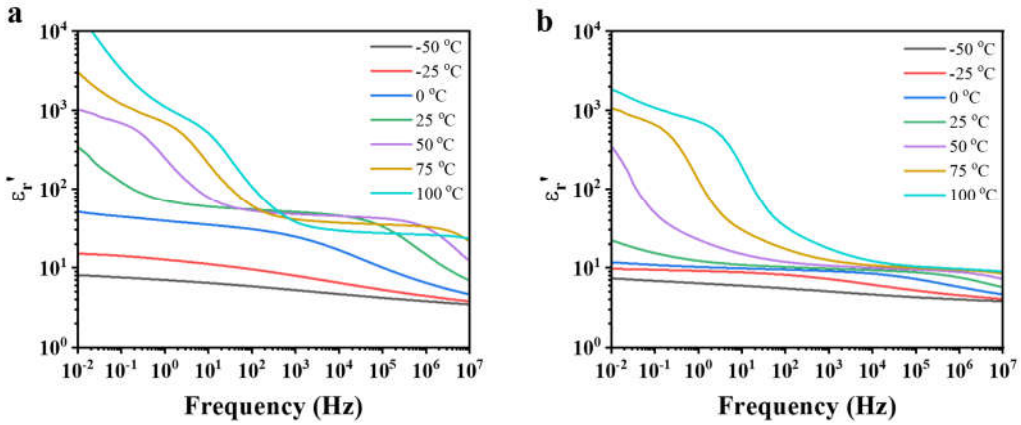

Figure S7. Real part (ε_r') of relative permittivity as a function of frequencies at different temperature for (a) *d*-PVDF and (b) PVDF.

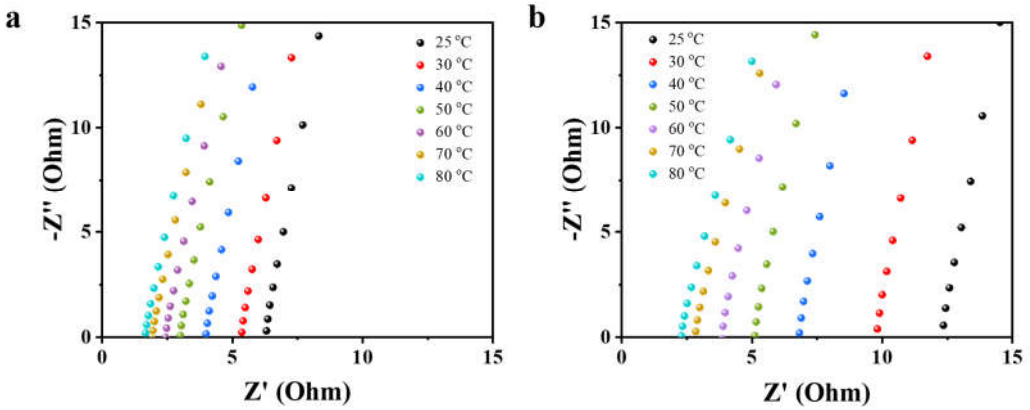

Figure S8. EIS curves of (a) *d*-PVDF SPEs and (b) PVDF SPEs sandwiched by two stainless plates of steel (SS) at different temperatures.

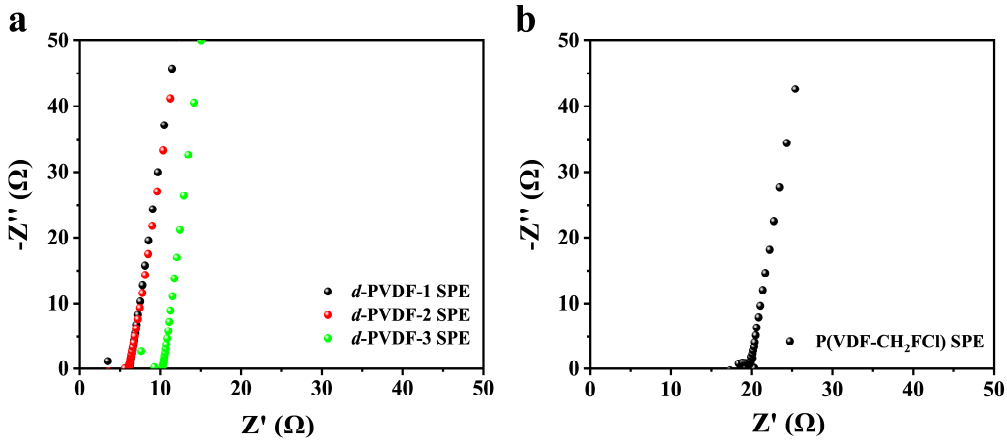

Figure S9. (a) EIS curves of different SPEs sandwiched by two stainless plates of steel (SS) at varying molar ratio of CHF_3 and CH_2FCl defects. (b) EIS curve of P(VDF-CH_2FCl) SPE sandwiched by two stainless plates of steel (SS) at room temperatures.

Table S2. The ionic conductivity of different SPEs at room temperature.

Sample name	Film thickness (μm)	Impedance (Ω)	Ionic conductivity (S cm^{-1})
P(VDF-CHF_3-CH_2FCl) 65.4/33.7/1.0 mol% (*d*-PVDF-1) SPE	76	6.2	6.13×10^{-4}
P(VDF-CHF_3-CH_2FCl) 62.5/33.3/4.2 mol% (*d*-PVDF-2) SPE	63	6.1	5.17×10^{-4}
P(VDF-CHF_3-CH_2FCl) 62.4/32.4/5.2 mol% (*d*-PVDF-3) SPE	95	11.2	4.23×10^{-4}
P(VDF-CH_2FCl) SPE	110	19.6	2.78×10^{-4}
P(VDF-CHF_3) SPE			4.48×10^{-4} S*(3)*

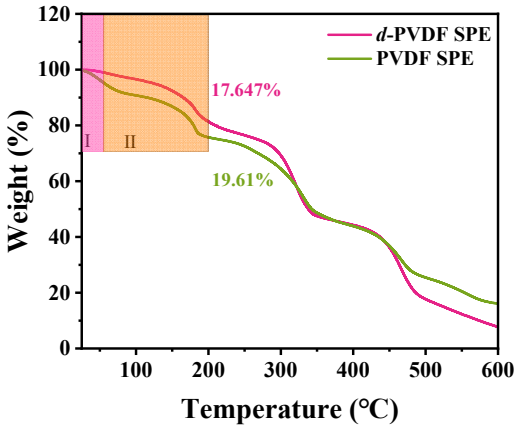

Figure S10. TGA curves of *d*-PVDF SPEs and PVDF SPEs. The minor weight loss before 55 °C (region I) comes from the evaporation of the trapped moisture, and the weight loss between 55 and 200 °C is ascribed to the residual DMF.

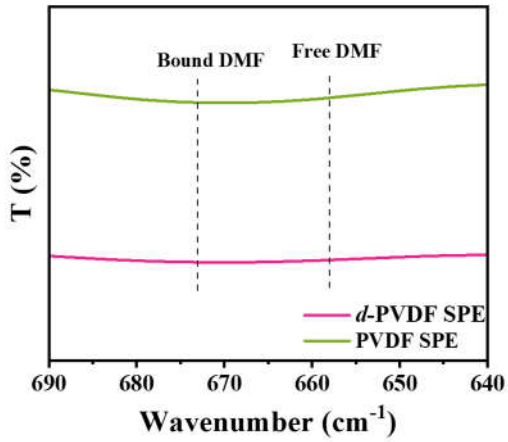

Figure S11. FTIR spectra of DMF molecules in *d*-PVDF SPEs and PVDF SPEs. The peak position for free and bound DMF locates at 658 and 673 cm^{-1}, respectively.

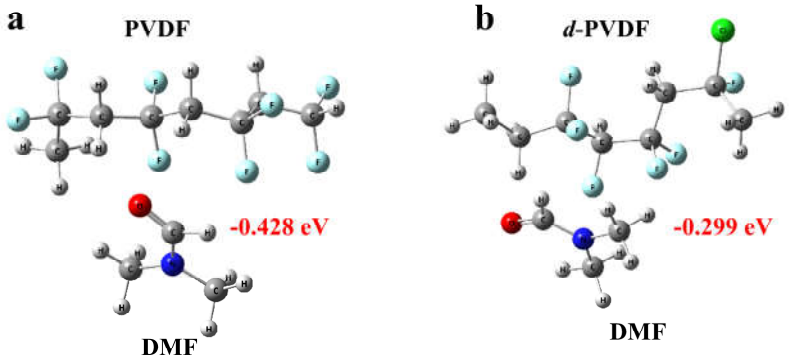

Figure S12. The interaction between DMF and (a) PVDF and (b) *d*-PVDF.

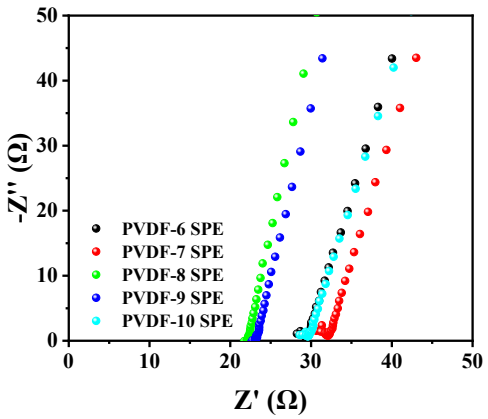

Figure S13. The ionic conductivity of PVDF SPEs with ~17% residual DMF at room temperature.

Table S3. The ionic conductivity of PVDF SPEs with ~17% residual DMF at room temperature.

Sample name	Film thickness (μm)	Impedance (Ω)	Ionic conductivity (S cm^{-1})
PVDF-6 SPE	118	29.6	2.0×10^{-4}
PVDF-7 SPE	108	32	1.7×10^{-4}
PVDF-8 SPE	101	22.3	2.3×10^{-4}
PVDF-9 SPE	105	23.6	2.3×10^{-4}
PVDF-10 SPE	116	29.4	2.0×10^{-4}

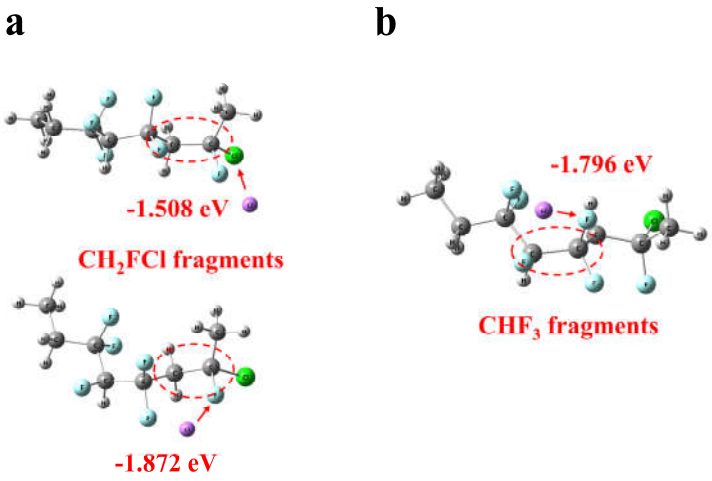

Figure S14. (a) The adsorption energy of Cl atom and F atom on CH_2FCl for lithium ions. (b) The adsorption energy of F atom on CHF_3 for lithium ions.

Table S4. The adsorption energy of lithium ions at different sites on CH_2FCl and CHF_3 fragments.

Monomer	Atom	Adsorption energy (eV)	Average adsorption energy (eV)
CH_2FCl	F	-1.872	-1.69
	Cl	-1.508	
CHF_3	F	-1.796	-1.79

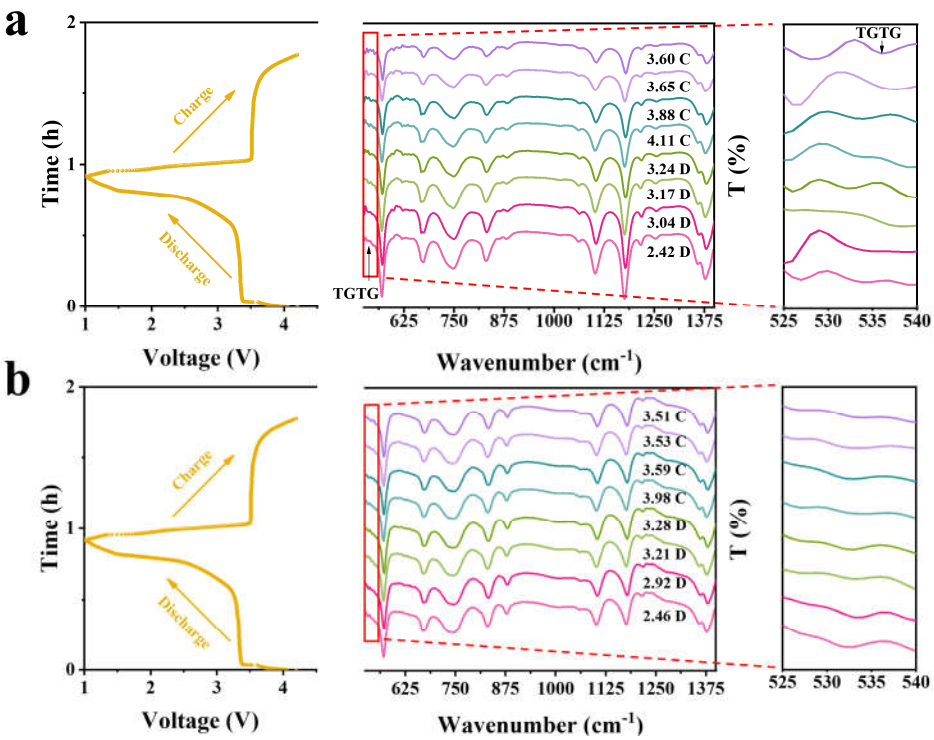

Figure S15. In-situ FTIR curves of (a) *d*-PVDF SPE and (b) PVDF SPE at different charging/discharging states of LFP//Li cells at 1 C and 25 °C.

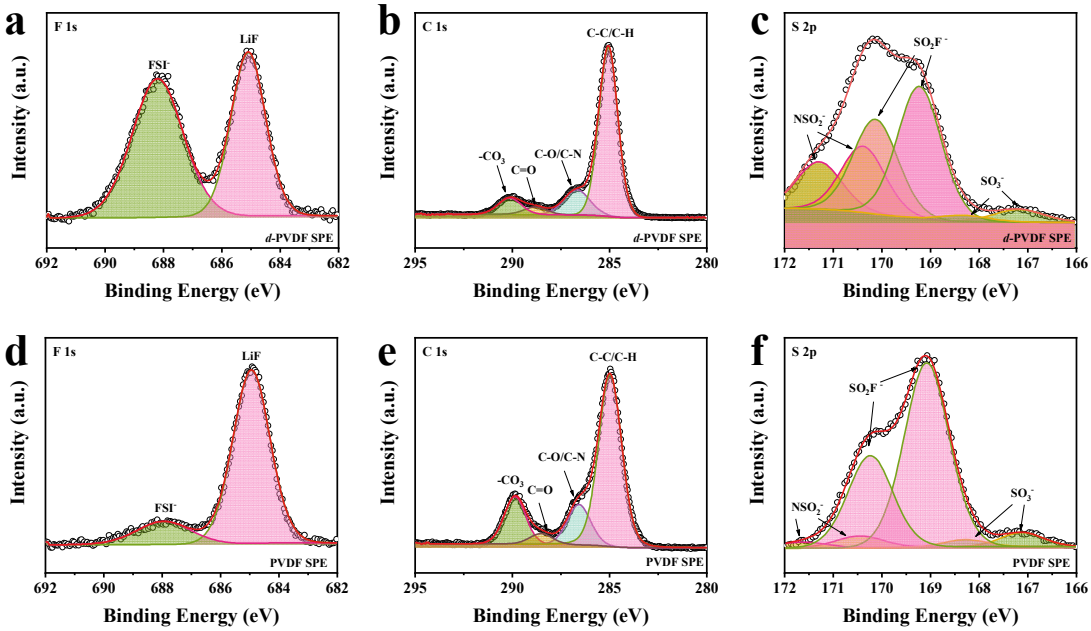

Figure S16 XPS spectra for (a, d) F 1s, (b, e) C 1s and (c, f) S 2p of cycled Li anode with (a, b, c) *d*-PVDF SPE and (d, e, f) PVDF SPE.

From Figure S16a and Figure S16d, LiF was formed in both cells that can benefit the stable cycling performance. Compared to the PVDF/Li interface (Figure S16d and Figure S16f), the *d*-PVDF SPE/Li interface contains more amount of FSI^- in F 1s spectrum (Figure S16a) and more NSO_2^- species in the S 2p spectrum (Figure S16c). Since the XPS sample was rinsed by DMC to remove any residual LiFSI, the more amount of FSI^- and NSO_2^- species in the *d*-PVDF SPE/Li interface should come from the decomposition of lithium salts during the cell cycling *(1-2)*. These results indicate that more lithium salts were dissociated in the *d*-PVDF SPE during the lithium deposition and stripping, which helps to improve the ionic conductivity.

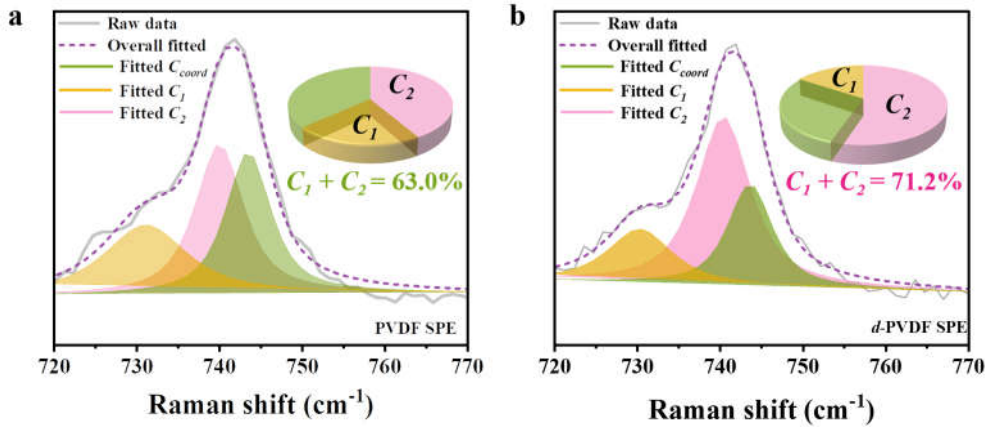

Figure S17. Raman spectra of (a) PVDF SPE and (d) *d*-PVDF SPE at 25 °C in the range of 720-770 cm^{-1}.

The amount of free Li^+ was examined by Raman testing. As shown in Figure S17a and S17b, three conformations, i.e. C_1 (cisoid), C_2 (transoid), and C_{coord}, were obtained by fitting the Raman peak at ~741 cm^{-1}, where C_1 and C_2 derive from the free FSI^-, and C_{coord} stems from the coordinated FSI^- with Li^+.*(30)* The sum proportion of C_1 and C_2 is 71.2% for *d*-PVDF SPE (Figure S17a), which is slightly higher than that of PVDF SPE (63.0%, Figure S17b), suggesting there are a greater number of free Li^+ in *d*-PVDF SPE.

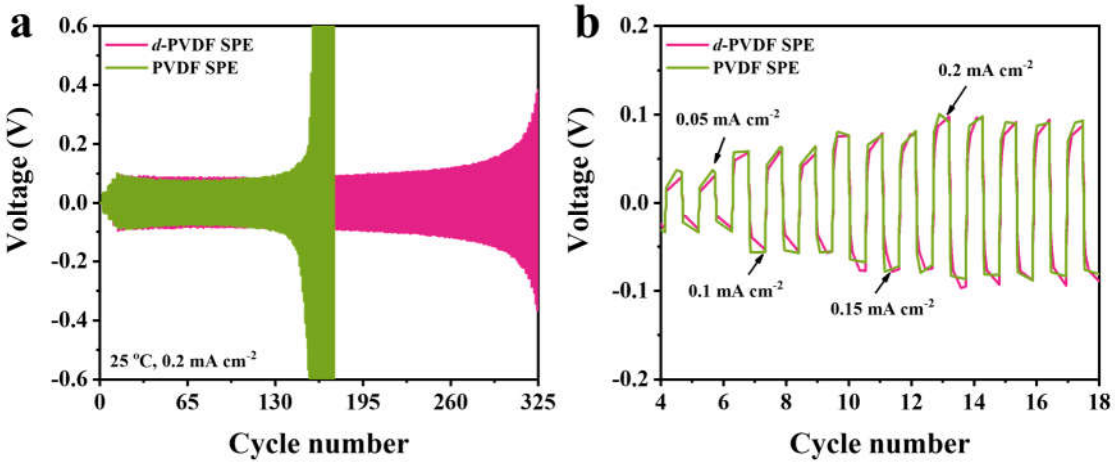

Figure S18. (a) Long cycling performance of Li/*d*-PVDF SPE/Li and Li/PVDF SPE/Li symmetrical cells at 25 °C under a current density of 0.2 mA cm^{-2} and (b) the enlarged view of initial cycles in (a). The charge/discharge time is 30 min.

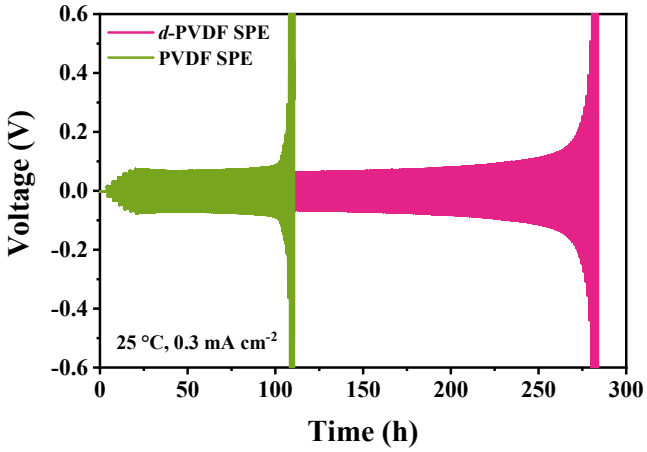

Figure S19. Long cycling performance of Li/*d*-PVDF SPE/Li and Li/PVDF SPE/Li symmetrical cells at 25 °C under a current density of 0.3 mA cm^{-2}.

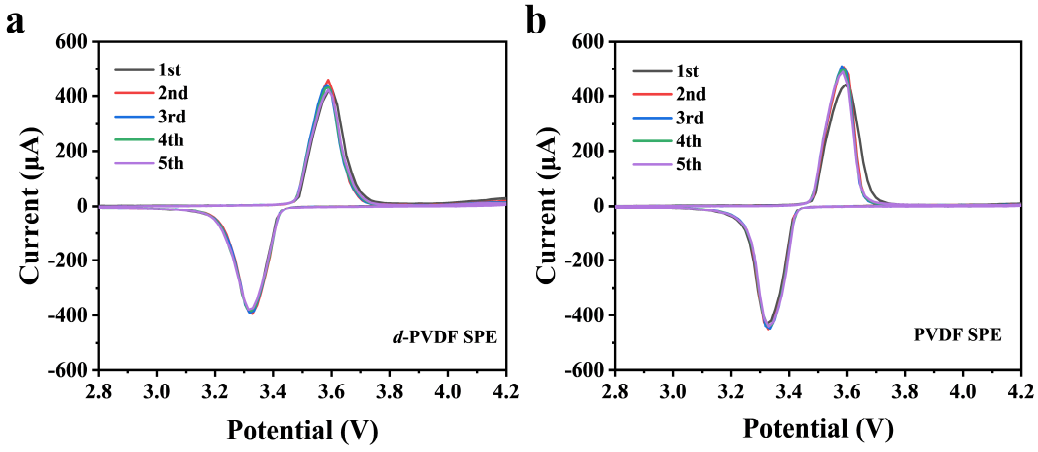

Figure S20. The CV curves of LFP//Li cells based on (a) *d*-PVDF SPE, and (b) PVDF SPE.

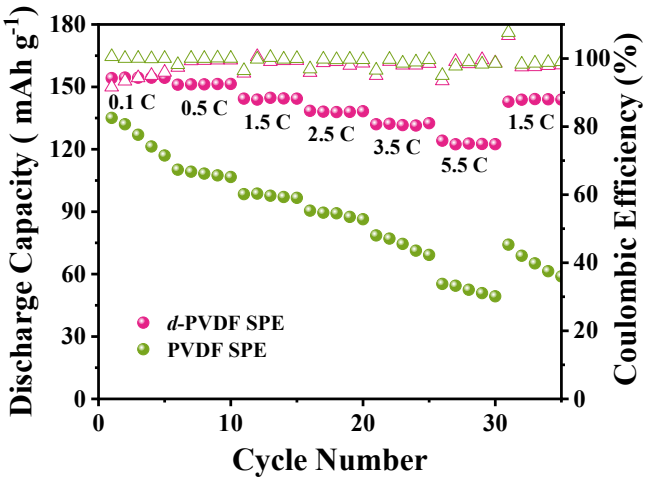

Figure S21. Discharge rate capability over a wide range of discharge current densities (0.1 C-5.5 C) of LFP/*d*-PVDF SPE/Li and LFP/PVDF SPE/Li cells.

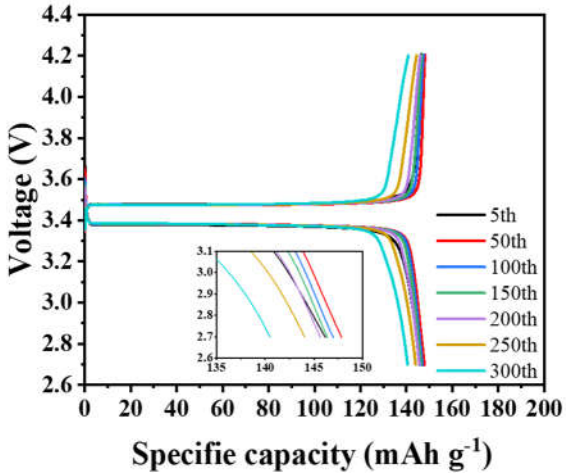

Figure S22. Charge/discharge curves of LFP/*d*-PVDF SPE/Li cells at 1C and 25 ºC.

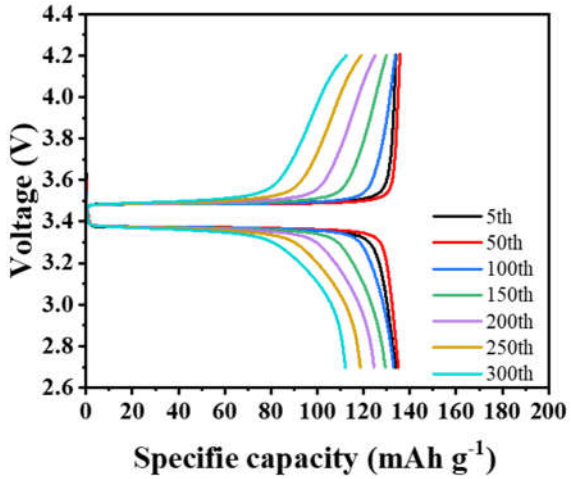

Figure S23. Charge/discharge curves of LFP/PVDF SPE/Li cells at 1 C and 25 ºC.

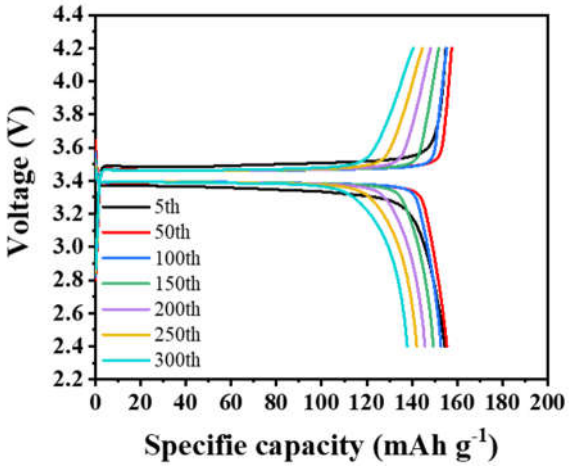

Figure S24. Charge/discharge curves of LFP/LEs/Li cells at 1 C and 25 ºC.

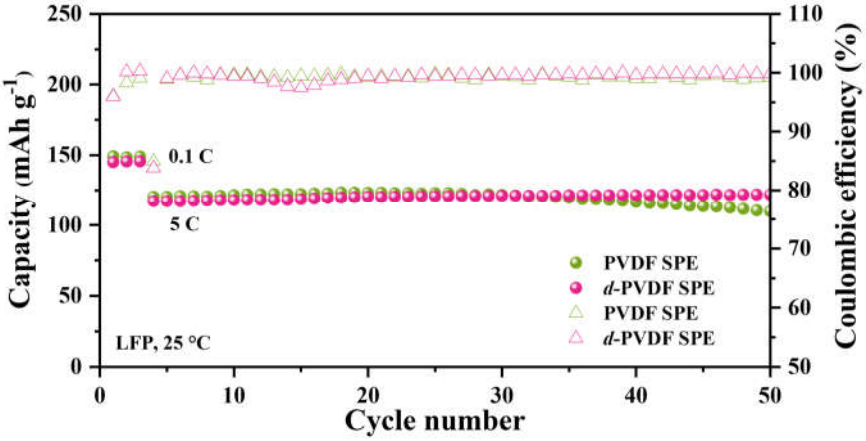

Figure S25. The enlarged view of Figure 5d.

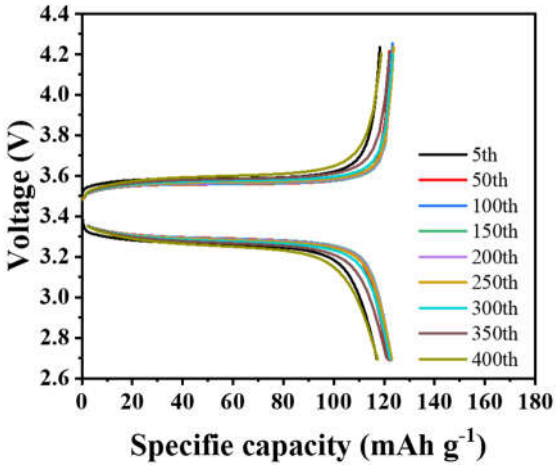

Figure S26. Charge/discharge curves of LFP/*d*-PVDF SPE/Li cells at 5 C and 25 ºC.

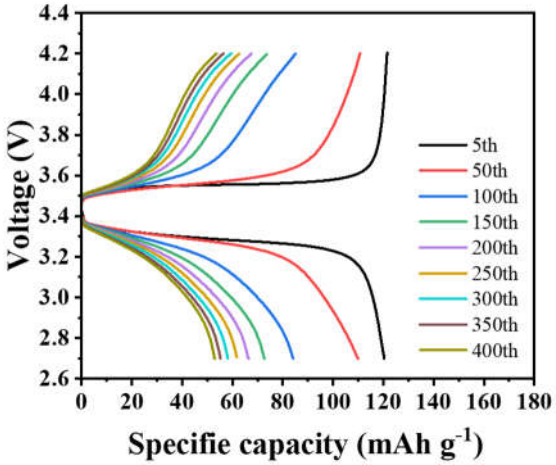

Figure S27. Charge/discharge curves of LFP/PVDF SPE/Li cells at 5 C and 25 ºC.

Table S5. Comparison of LFP//Li battery performance with reported results in literatures.

SPEs	Ionic conductivity (10^{-4} S/cm)	Cycle rate	Capacity retention	Ref
d-PVDF/LiFSI	7.8 at 25 ºC	5 C	100.0% at 400 cycles	**This work**
PVDF-HFP/MOF composite gel	2.0 at 25 ºC	0.2 C	87.3% at 200 cycles	S*(5)*

/$Li_{6.75}La_3Zr_{1.75}Nb_{0.25}O_{12}$ nanowires/LiTFSI				
PVDF-HFP/$Li_{6.28}Al_{0.24}La_3Zr_2O_{12}$/ h-BN/LiTFSI	0.7 at 25 ºC	0.2 C	92.0% at 100 cycles	S*(6)*
PAN-PEO/LiTFSI	0.05 at 25 ºC	0.3 C	69.6% at 300 cycles (60 ºC)	S*(7)*
Poly (ethylene glycol) diacrylate (PEGDA) /MMT/LiTFSI	10.6 at 25 ºC	0.3 C	>98.0% at 400 cycles	S*(8)*
PEO/LLZTO/LiTFSI	1.58 at 25 ºC	0.5 C	97.1% at 400 cycles	S*(9)*
M-S-PEGDA/LiTFSI	2.3 at 25 ºC	0.5 C	87.0% at 400 cycles	S*(10)*
PEO/PEG/$Li_{10}GeP_2S_{12}$/ LiTFSI	9.8 at 25 ºC	0.5 C	91.0% at 150 cycles	S*(11)*
PEO-1 wt% I_2/LiTFSI	0.72 at 50 ºC	0.5 C	96.5% at 300 cycles (50 ºC)	S*(12)*
PVDF-HFP/ PEO/LLZO/LiTFS	2.5 at 80 ºC	0.1 C	99.0% at 80 cycles (50 ºC)	S*(13)*
PAN-LLZTO/LiTFSI	20.6 at 25 ºC	2 C	88.9% at 200 cycles	S*(14)*
PVDF/LLZTO/LiTFSI	2.4 at 25 ºC	1 C	88.0% at 200 cycles	S*(15)*
Si@LATP/PVDF/PVC/ LiTFSI	1.06 at 25 ºC	1 C	94.1% at 200 cycles	S*(16)*
PVDF-HFP/LLZTO/LiFSI	16.7 at 25 ºC	0.5 C	97.2% at 300 cycles	S*(17)*

PEO/LLZTO@IL/ LiTFSI	1.0 at 60 °C	0.2 C	96.2% at 100 cycles	S*(18)*
P(VDF-TrFE-CTFE)/ LiTFSI	3.1 at 25 °C	0.5 C	98.5% at 150 cycles	S*(19)*

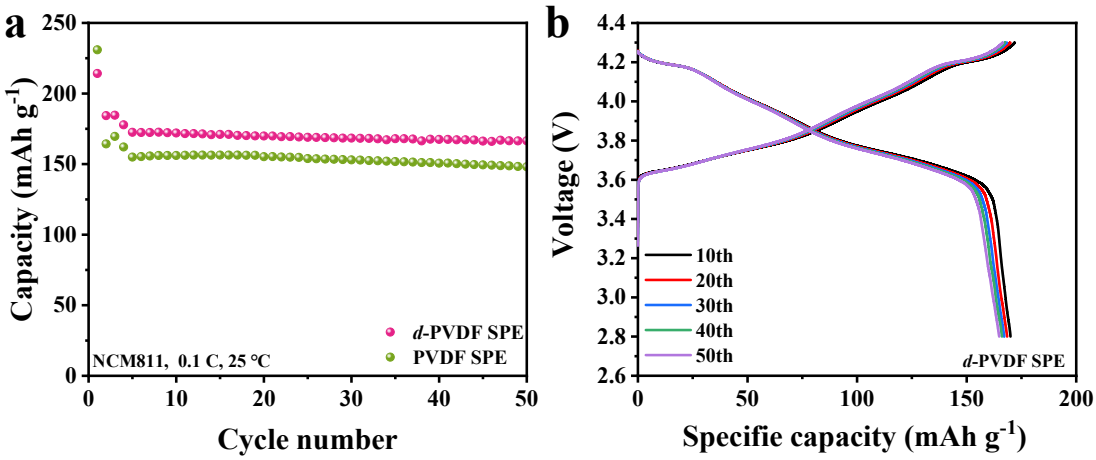

Figure S28. Cycling performance of (a) NCM811/*d*-PVDF SPE/Li batteries at 0.1 C and 25 °C, and (b) the corresponding charge/discharge curves.

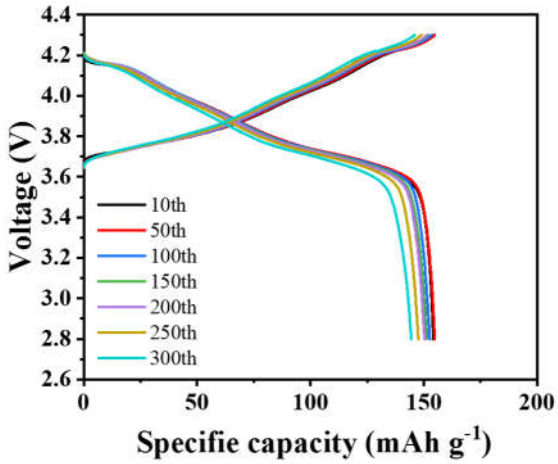

Figure S29. Charge/discharge curves of NCM811/*d*-PVDF SPE/Li cells at 1 C and 25 °C.

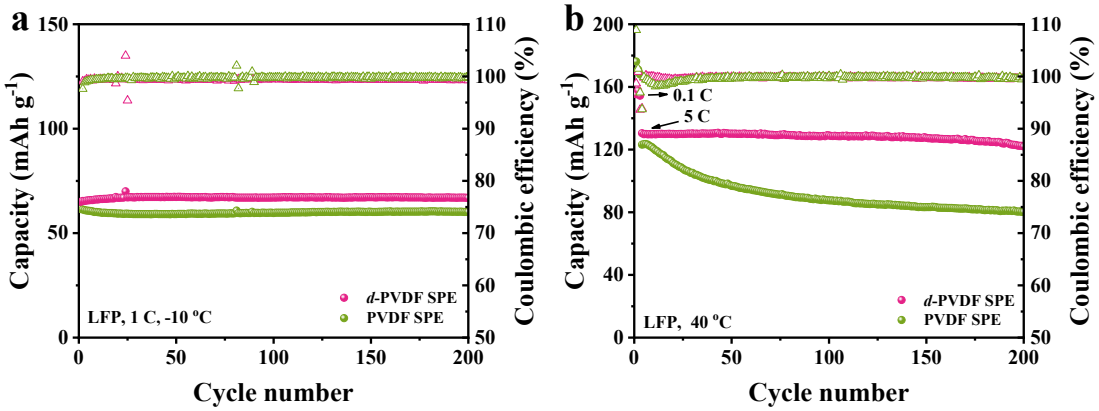

Figure S30. Long-term cycling performance of LFP//Li cells at (a) 1 C , -10 °C and (b) 5 C, 40 °C.

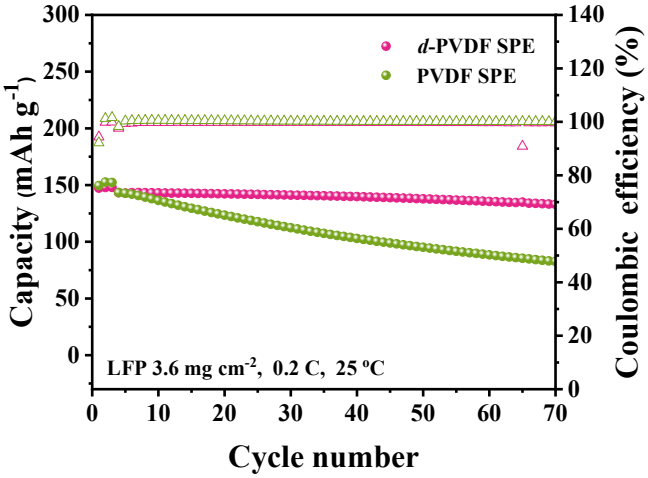

Figure S31. Cycling performances of LFP/*d*-PVDF SPE/Li and LFP/PVDF SPE/Li cells with a cathode mass loading of 3.6 mg cm^{-2} at the rate of 0.2 C at 25 ℃. The PVDF binder was replaced by P(VDF-TrFE).

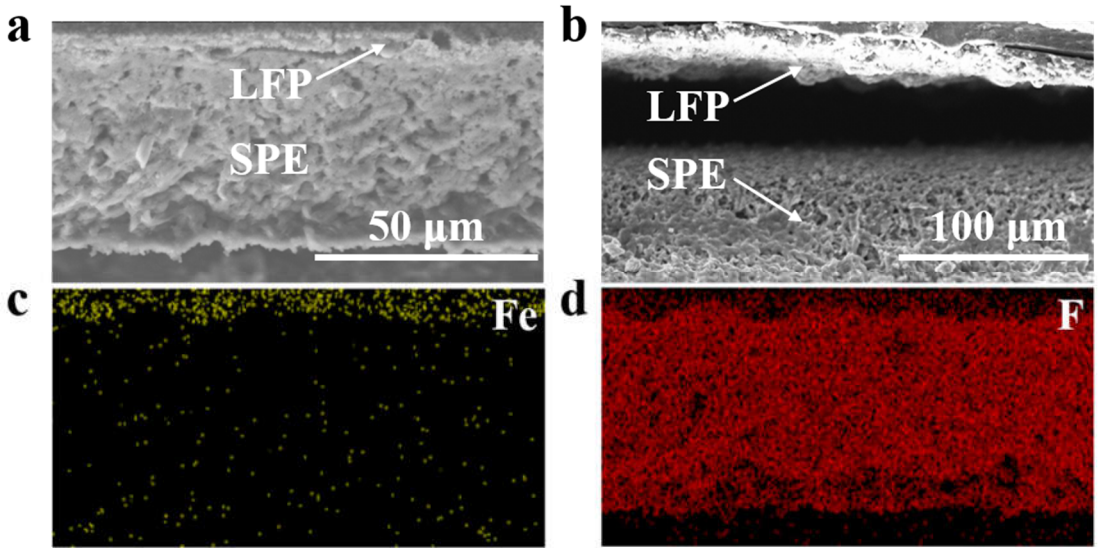

Figure S32. The cross-sectional SEM image of the (a) LFP/*d*-PVDF SPE/Li and (b) LFP/ PVDF SPE/Li cells after 100 cycles at 5 C and 25 ºC and (c, d) the energy dispersive spectroscopy (EDS) maps of (a).

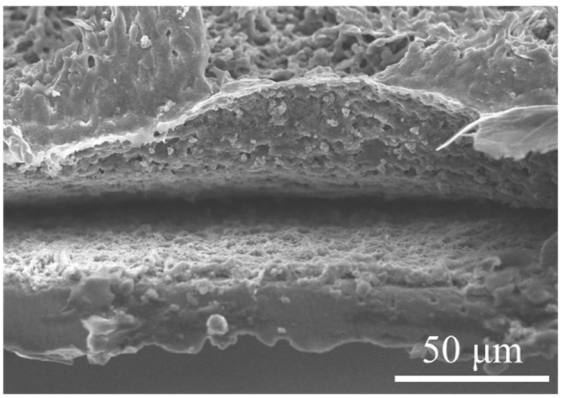

Figure S33. The cross-sectional morphology of the interface of NCM811/PVDF SPE from cycled NCM811//Li batteries after 50 cycles at 1 C and 25 ºC.

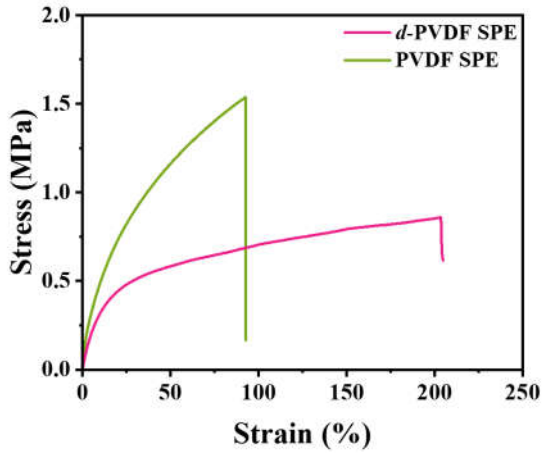

Figure S34. Tensile properties of *d*-PVDF SPEs and PVDF SPEs.

References

1. I. A. Shkrob *et al.*, Why bis(fluorosulfonyl)imide is a "Magic Anion" for electrochemistry. *J. Phys. Chem. C* **118**, 19661-19671 (2014).
2. W. Gu et al., Lithium-iron fluoride battery with in situ surface protection. *Adv. Funct. Mater.* **26**, 1507-1516 (2016).
3. J. P. Zeng *et al.*, A high polarity poly(vinylidene fluoride-co-trifluoroethy lene) randomcopolymer with an all-trans conformation for solid-state LiN $i_{0.8}Co_{0.1}Mn_{0.1}O_2$/lithium metal batteries. *J. Mater. Chem. A.* **10**, 18061-18 069 (2022).
4. V. Amoli *et al.*, A bioinspired hydrogen bond-triggered ultrasensitive ionic mechanoreceptor skin. *Nat. Commun.* **10**, 4019 (2019).
5. J. Sun *et al*., Facilitating interfacial stability via bilayer heterostructure solid electrolyte toward high-energy, safe and adaptable lithium batteries. *Adv. Energy Mater*. **10**, 2000709 (2020).
6. J. H. Kim *et al.*, High-performance free-standing hybrid solid electrolyte membrane combined with $Li_{6.28}Al_{0.24}La_3Zr_2O_{12}$ and hexagonal-BN for all-solid-state lithium-based batteries. *Chem. Eng. J.* **446**, 137035 (2022).
7. Y. X. Ma *et al.*, Scalable, ultrathin, and high-temperature-resistant solid polymer electrolytes for energy-dense lithium metal batteries. *Adv. Energy Mater.* **12**, 2103720 (2022).
8. Y. Wang *et al.*, Local electric field effect of montmorillonite in solid polymer electrolytes for lithium metal batteries. *Nano Energy* **90**, 106490 (2021).
9. C. Song *et al.*, Enhancing Li ion transfer efficacy in PEO-based solid polymer electrolytes to promote cycling stability of Li-metal batteries. *J. Mater. Chem. A* **10**, 16087-16094 (2022).
10. H. C. Wang *et al.*, Thiol-branched solid polymer electrolyte featuring high strength, toughness, and lithium ionic conductivity for lithium-metal batteries. *Adv. Mater.* **32**, 2001259 (2020).

11. K. C. Pan *et al.*, A flexible ceramic/polymer hybrid solid electrolyte for solid-state lithium metal batteries. *Adv. Mater.* **32**, 2000399 (2020).
12. O. W. Sheng *et al.*, Interfacial and ionic modulation of poly (ethylene oxide) electrolyte via localized Iodization to enable dendrite-free lithium metal batteries. *Adv. Funct. Mater.* **32**, 2111026 (2022).
13. G. X. Yu *et al.*, Plasma optimized $Li_7La_3Zr_2O_{12}$ with vertically aligned ion diffusion pathways in composite polymer electrolyte for stable solid-state lithium metal batteries. *Chem. Eng. J.* **430**, 132874 (2022).
14. Z. H. Ren *et al.*, Insight into the integration way of ceramic solid-state electrolyte fillers in the composite electrolyte for high performance solid-state lithium metal battery. *Energy Storage Mater.* **51**, 130-138 (2022).
15. S. S. Zhang *et al.*, Room-temperature, high-voltage solid-state lithium battery with composite solid polymer electrolyte with in-situ thermal safety study. *Chem. Eng. J.* **400**, 125996 (2020).
16. Y. M. Jin *et al.*, Constructing 3D Li^+-percolated transport network in composite polymer electrolytes for rechargeable quasi-solid-state lithium batteries. *Energy Storage Mater.* **49**, 433-444 (2022).
17. J. M. Zhang *et al.*, Polymer-in-salt electrolyte enables ultrahigh ionic conductivity for advanced solid-state lithium metal batteries. *Energy Storage Mater.* **54**, 440-449 (2023).
18. C. L. Deng *et al.*, Enhancing interfacial contact in solid-state batteries with a gradient composite solid electrolyte. *Small* **17**, 2006578 (2021).
19. Y.-F. Huang *et al.*, A relaxor ferroelectric polymer with an ultrahigh dielectric constant largely promotes the dissociation of lithium salts to achieve high ionic conductivity. *Energy Environ. Sci.* **14**, 6021-6029 (2021).